
Imaging the Cold, Compressed Shell in Laser Implosions Using the $K\alpha$ Fluorescence of a Titanium Dopant

The cold, compressed shell in laser-driven implosions can normally be imaged only by backlighting because its x-ray emission is very weak. However, a high- Z -doped shell can be imaged using the $K\alpha$ line radiation, which fluoresces due to excitation by the intense radiation from the hot core. We show results from titanium-doped target implosions where the one-dimensional spatial profile of the Ti $K\alpha$ radiation yields the dimensions of the cold shell around the time of peak compression. This result, coupled with the shell areal density determined by the K -edge absorption, yields an estimate of the shell density. Since $K\alpha$ emission depends only on the cold shell density (not its temperature), its image directly reflects the shell uniformity. Additionally, the measured absorption above the K -edge and the energy in the $K\alpha$ line, which are directly related, are shown to indeed be consistent.

Laser-imploded targets consist of a hot core surrounded by a cold, compressed shell. Diagnosing the shell is vital to understanding target implosion, and several x-ray-based methods have been developed to address this requirement. For example, it has been shown^{1,2} that the peak in the emergent continuum radiation (caused by shell absorption of the soft radiation) can be used to determine the shell areal density. More recently^{3,4} it has been shown that doping part of the shell with a high- Z element provides additional signatures of shell temperature and areal density, namely, absorption lines and K -edge absorption [including extended x-ray absorption fine structure (EXAFS)]. All these methods depend on the core radiation; thus, a time-integrated measurement yields approximately the conditions at peak compression, when that radiation is strongest.

Additional valuable information can be provided by imaging the cold shell. Since a cold shell emits few x rays, its imaging is normally done by backlighting.⁵⁻⁷ However, we show in this article that when the cold shell is doped, it can be imaged using $K\alpha$ fluorescence excited by the core radiation. The fluorescence of $K\alpha$ radiation can occur only in cold material and is significant only when the pumping core radiation is intense; thus, the $K\alpha$ emission profile delineates the

cold shell surrounding the hot core around the time of peak compression. The term “cold” in this context will be defined below. This imaging method is much simpler than backlighting and has an additional advantage: whereas in backlighting an intense core radiation competes with the signal, here, to the contrary, it enhances it. $K\alpha$ emission in past experiments has been associated with excitation by suprathreshold electrons⁸ or by coronal radiation.⁹ However, the data in the present experiment clearly shows that the excitation source for the $K\alpha$ line is the core radiation.

$K\alpha$ fluorescence can be imaged by monochromatic, two-dimensional imaging; a method involving a Kirkpatrick–Baez (KB) microscope coupled to a diffracting crystal was recently demonstrated by Marshall and Oertel.¹⁰ Here we report on one-dimensional polychromatic imaging obtained with a crystal spectrograph fitted with a spatially resolving slit. One-dimensional imaging cannot show the symmetry of the cold shell, but it can determine its average radial extent. Coupled with the measurement of the shell’s areal density by any of the above methods, this result can lead to an estimate of the average shell density around peak compression. Also, the measured spatial extent of $K\alpha$ radiation provides an additional constraint on two- and three-dimensional simulations of target implosion. The purpose of this work is to demonstrate that $K\alpha$ images can be obtained with targets of low-level doping and that a cold shell is indeed found to surround the hot, compressed core.

Experimental Results

Figure 72.6 shows a schematic of the target and measurement configurations. The polymer target is initially empty; at peak compression, part of the overcoat has been ablated and the inner part of the mandrel forms the core. The doped layer contains titanium at 0.5% by atom number. An axial view by the x-ray spectrometer shows the emission of continuum from the core, as well as K -edge absorption and $K\alpha$ emission within the doped layer. *An off-axis view should show only the $K\alpha$ emission.* The overcoat is much thicker than the laser-ablated layer, ensuring that none of the titanium-doped layer is ablated away. Likewise, the titanium layer is sufficiently far from the

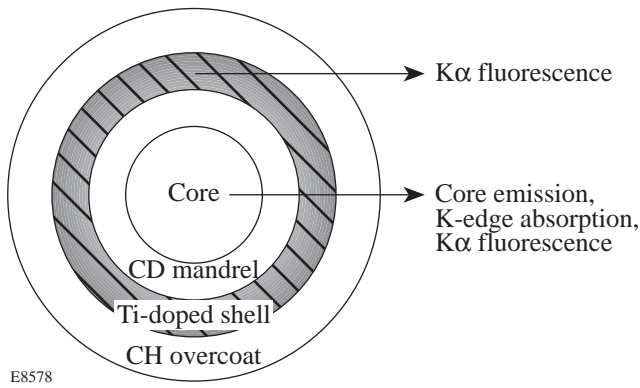


Figure 72.6

Schematic representation of the target and measurement configurations. An axial view by the x-ray spectrometer shows the core emission of continuum as well as K -edge absorption and $K\alpha$ emission within the doped layer. An off-axis view shows only the $K\alpha$ fluorescence emission.

inner-shell interface to ensure no emission of titanium lines in the absence of mixing.⁴ The titanium layer is thus cold for the most part and should give rise to $K\alpha$ fluorescence.

We analyze the results from a single target shot, No. 9095, on the OMEGA laser system.¹¹ The target was a $6.1\text{-}\mu\text{m}$ -thick, empty CD mandrel of $931\text{-}\mu\text{m}$ outer diameter, coated with a $8.7\text{-}\mu\text{m}$ -thick CH shell that was doped with titanium at 0.5% concentration by atomic number (or at a density of 0.037 g/cm^3). Finally, the target was overcoated with an $18.7\text{-}\mu\text{m}$ -thick CH layer. The 29.6-kJ laser pulse had a 1-ns flat top (to within $\pm 5\%$) with 100-ps rise and fall times. Smoothing by spectral dispersion (SSD)¹² was used in this experiment, but not distributed phase plates (DPP's).¹³

The x-ray spectrum in the range of ~ 4 to 9 keV was recorded by a Ge(111) crystal spectrometer fitted with a $100\text{-}\mu\text{m}$ -wide spatially resolving slit. The crystal and film calibration methods used in the data reduction are explained in Ref. 4. Spectrally dispersed images were also obtained with a KB x-ray microscope of resolution $\leq 5\text{ }\mu\text{m}$, fitted with a dispersing grating, similar to the arrangement described by Marshall *et al.*² The KB microscope mirrors are coated with iridium rather than gold.¹⁰ The dispersion of the grating was $0.97\text{ }\text{\AA}/\text{mm}$ (insufficient for resolving spectral lines), and the image magnification was 12.5.

Figure 72.7 shows part of the spectrum (in the axial view) containing the main features of interest in this work: the $K\alpha$ line and the K -edge absorption. The absorption of core emission seen above the K -edge leads to $K\alpha$ excitation. By quanti-

tatively relating the two we can verify that the absorption of core radiation accounts for all the energy in the $K\alpha$ line. The rapid changes in absorption above the K -edge are related to EXAFS.⁴ Also, the narrow spike of absorption at the K -edge has been observed in synchrotron experiments on titanium¹⁴ and other metals¹⁵ and is attributed to a high density of d -orbital states above the Fermi level. The Ti He- α line (along with its dielectronic satellites) is a signature of mixing.⁴ Earlier experiments with thinner, Ti-doped shells⁴ showed absorption lines due to $1s\text{-}2p$ transitions in Ti ions with various L -shell vacancies (in addition to K -edge absorption); the absence of these lines in Fig. 72.7 indicates that the doped layer is uniformly cold ($T \leq 100\text{ eV}$).

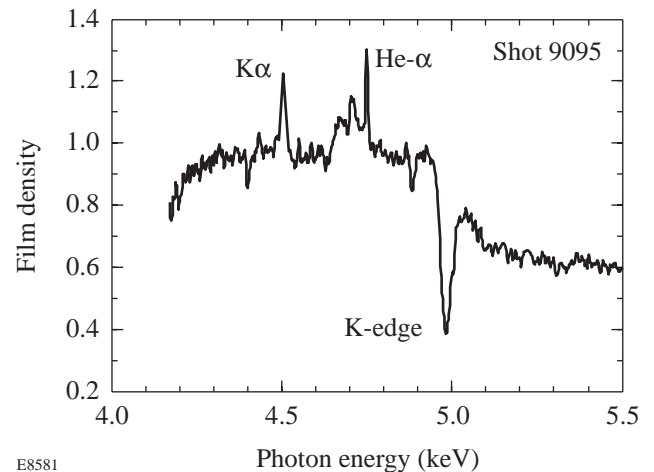


Figure 72.7

Detailed view of the significant spectral features in the spectrum. The Ti $K\alpha$ line is emitted by the cold titanium-doped layer due to excitation by the core radiation. Above the K -edge the continuum level is seen to drop because of absorption by the same layer emitting the $K\alpha$ line. The Ti He- α line (along with its dielectronic satellites) is a signature of mixing.⁴

1. Temperature and Areal Density Determinations

The drop in intensity above the K -edge of cold titanium at 4.966 keV enables us to estimate the temperature of the absorbing titanium layer. To that end we show in Fig. 72.8 the change in the Ti K -edge energy when successive outer electrons are removed.¹⁶ When the 12 M -shell electrons in Ti are removed, the edge shifts progressively from 4.966 keV up to $\sim 5.3\text{ keV}$; when the eight L -shell electrons are removed, the edge shifts progressively from ~ 5.3 to $\sim 6.2\text{ keV}$. Thus, a distribution of charge states would cause the intensity above the edge to decline gradually, rather than abruptly. The solid-state features near the K -edge (which may mask such a decline) extend over $\sim 150\text{ eV}$; we can therefore state that up to ~ 5 electrons could have been ionized. Using a collisional-

radiative steady-state calculation this can be shown to correspond to a temperature in the doped layer of less than ~40 eV. This is consistent with the above-mentioned absence of absorption lines, which would have required³ a higher temperature ($T \sim 200$ to 500 eV).

We now derive the areal density of the titanium shell using the absorption above the K -edge. The solid-state features near the K -edge obscure the drop in intensity at the edge. Consequently, in fitting the experimental spectrum with standard cold opacity data (which do not include these K -edge features),

we rely on a wide range of the spectrum *away from the K -edge*. We show in Fig. 72.9 the total measured spectrum, in axial view, after subtracting the background due to coronal emission (see Fig. 72.10). Starting with the observed spectrum $I(E)$ we derive the spectrum $I_c(E)$ emitted by the core before being attenuated by the cold titanium layer. This is given simply by

$$I_c(E) = I(E) / \exp[-\rho\Delta r \tau(E)], \quad (1)$$

where $\rho\Delta r$ is the areal density of the titanium alone and $\tau(E)$ is the absorption (or opacity) of cold titanium. We adjust $\rho\Delta r$

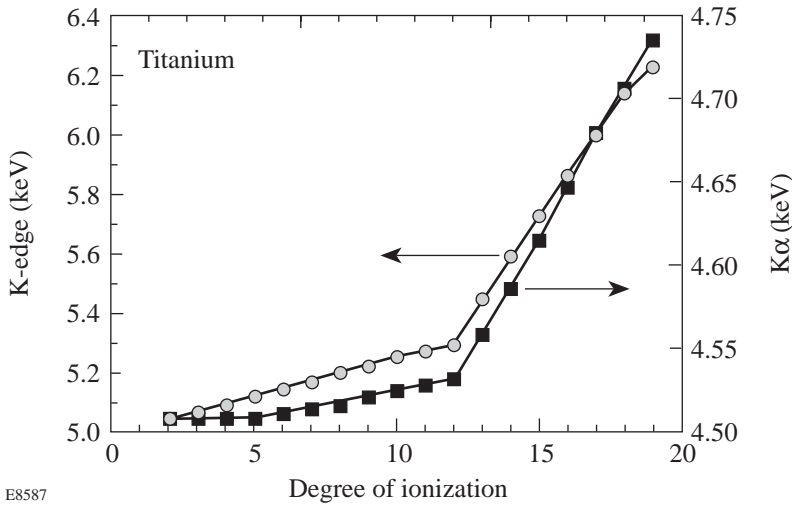


Figure 72.8
The shift of the Ti K -edge and Ti $K\alpha$ energies with the removal of successive electrons by ionization.

E8587

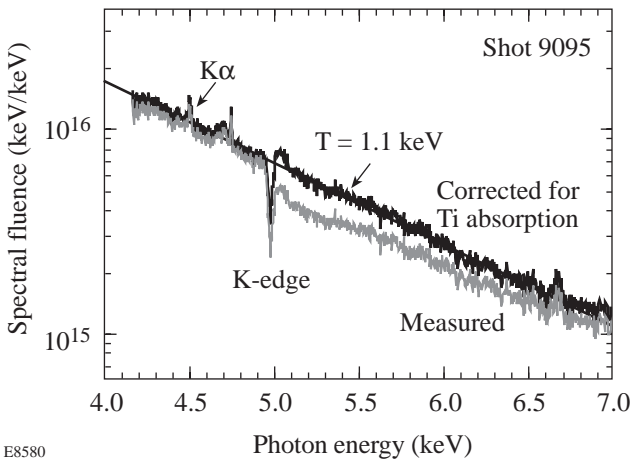


Figure 72.9
Axial view of the calibrated spectrum showing the core continuum emission (after subtracting the background due to coronal emission). The areal density of the titanium-doped layer is obtained by dividing the observed spectrum by the opacity of cold titanium: a layer of $\rho\Delta r = (16 \pm 1.6)$ mg/cm² results in an exponential curve that joins smoothly the spectrum below the K -edge. The slope yields the core temperature.⁴

E8580

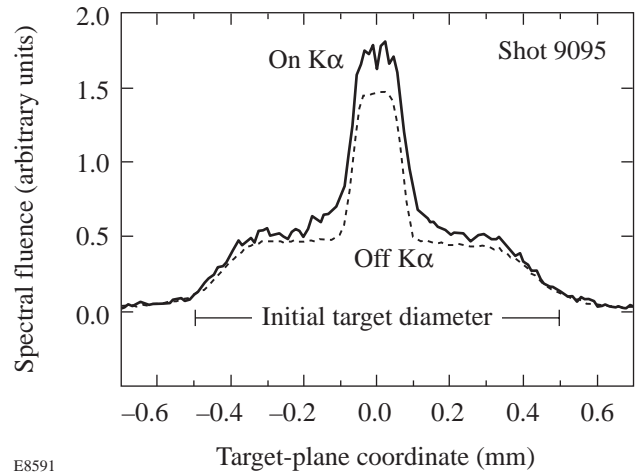


Figure 72.10
The one-dimensional image of target emission, in the target plane, averaged over a photon-energy interval of 0.1 keV on each side of the $K\alpha$ line. The core emission is clearly distinct from that of the laser-heated coronal region. Note that the 100- μ m-wide slit has in this image a magnification larger by a factor $(1+1/M) \sim 1.55$ than the target magnification M . The emission profile at the wavelength of the $K\alpha$ line is also shown.

E8591

until the resulting core-emitted spectrum smoothly joins the spectrum below the K -edge. The best fit is shown in Fig. 72.9 by the curve marked “corrected for Ti absorption.” The corresponding areal density of the titanium alone is (0.56 ± 0.05) mg/cm²; hence, the areal density of the doped layer is (16 ± 1.6) mg/cm². The error in the areal density is determined by the noise in the spectral intensity. Using this value we can estimate the total areal density of the compressed shell, using the value of total ablated target mass. Charge-collector data showed that a layer of thickness ~ 11 μm (of the initial target overcoat) has been ablated away, leaving ~ 23 μm unablated. It has been shown⁴ that the $\rho\Delta r$ ratio of the unablated shell to that of an embedded layer within the shell increases only slightly during the implosion (more so, the closer the embedded layer is to the inner surface of the shell); for our case this ratio increases by up to $\sim 30\%$ for increasing compression ratios. Furthermore, the ratio can be approximately calculated by assuming the shell to implode incompressibly (the increase in areal density is mostly due to the radial convergence, not the compression); thus, a lower limit of this ratio is given by its value in the initial target. For the present target this value is 2.6, leading to an estimate of the total shell areal density of ≈ 42 mg/cm². The slope of $I_c(E)$ indicates a core electron temperature of ~ 1.1 keV.

2. The Relationship between $K\alpha$ Emission and K -Edge Absorption

The absorption of core radiation seen above the K -edge can be used to calculate the energy in the $K\alpha$ line, which can then be compared with its measured value. The relationship between the two is given by the equation

$$\varepsilon(K\alpha) = 0.5 \exp[-\tau(CH)] E(K\alpha) \omega_K(Ti) \int_{E_K}^{\infty} [I(\text{measured}) - I(\text{corrected})] dE/E. \quad (2)$$

The integral calculates the total number of photons absorbed above the K -edge and is obtained directly from the difference between the two curves in Fig. 72.9. ω_K is the relative probability for an ion with a K -shell vacancy to decay by emitting a $K\alpha$ photon (the fluorescence yield). For neutral Ti the measured fluorescence yield is $\omega_K = 0.21$.¹⁷ When the outer electrons are successively removed, the fluorescence yield increases gradually.¹⁸ As discussed above, the titanium atoms in the cold shell could have up to five electrons ionized. We calculated ω_K for these ionic species using the model described by McGuire:¹⁹ by removing five M -shell electrons, ω_K increases gradually from 0.21 to 0.31. Since the number (five) of electrons ionized

is an upper limit, we use the value for neutral Ti (namely, 0.21) and obtain a lower bound on the expected $K\alpha$ energy. Figure 72.8 shows that the $K\alpha$ line emitted by these ions would shift by less than ~ 5 eV. The observed $K\alpha$ linewidth is in fact much larger than 5 eV (see below) and thus possibly includes the emission from all these ions. $E(K\alpha)$ in Eq. (2) is the photon energy of the $K\alpha$ line (~ 4.5 keV), and the factor 0.5 accounts for the fact that only half the $K\alpha$ photons travel outward. The correction factor in front of the integral accounts for absorption of $K\alpha$ photons in the polymer shell (the $K\alpha$ line cannot be resonantly absorbed since if the temperature is high enough to produce the required L -shell vacancy, it will surely be high enough to deplete the M shell). Using the above estimated areal density of the compressed shell, we obtain $\exp[-\tau(CH)] \sim 0.7$. Applying Eq. (2) to Fig. 72.9, we obtain for the predicted $K\alpha$ energy $\varepsilon(K\alpha) \sim (15 \pm 3)$ mJ. The error results from the noise in the spectrum and uncertainty in $\tau(CH)$. Measuring $\varepsilon(K\alpha)$ directly from Fig. 72.9 (integrating over the line profile), we obtain $\varepsilon(K\alpha) \sim (13 \pm 2)$ mJ. Since the measured value is lower than the predicted value (the latter being an underestimate), we conclude that the $K\alpha$ line is indeed excited primarily by core radiation. If, for example, coronal excitation played a significant role in exciting the $K\alpha$ line, the measured $\varepsilon(K\alpha)$ would exceed the value predicted by Eq. (2). This point is further supported below. The low measured value of $\varepsilon(K\alpha)$ also suggests that the shell temperature is well below 40 eV; otherwise, the increase of ω_K with ionization would increase the value of $\varepsilon(K\alpha)$ as determined by Eq. (2).

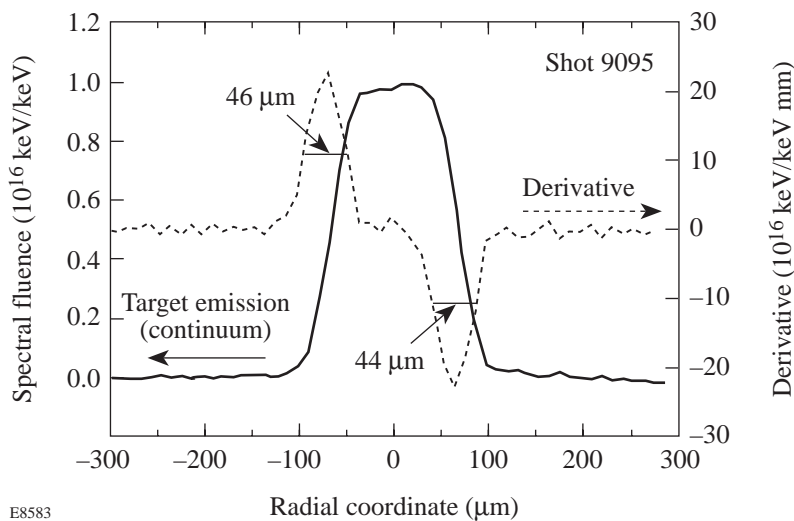
3. One-Dimensional Continuum and $K\alpha$ Target Images

One-dimensional images of the target emission in the range of ~ 4 to 9 keV were obtained by placing a slit in front of the crystal spectrometer. Because of the relatively large width of the slit (100 μm), the true core images will be derived by differentiating the measured slit images. Since the core emission is mostly a continuum, we select a narrow band of the continuum, close to the energy of the $K\alpha$ line, to characterize the core size. Figure 72.10 shows the calibrated one-dimensional image of target emission, averaged over a photon-energy interval of 0.2 keV (0.1 keV on each side of the $K\alpha$ line). The image is shown in the target plane, where the 100- μm -wide slit is magnified by a factor $(1+1/M) \sim 1.55$ in terms of the target magnification M . The core emission is clearly distinct from that of the laser-heated coronal region. Note that because the slit is wider than the core (see below) but narrower than the target, the coronal intensity is per slit width, whereas the central emission is integrated over the core volume. The emission profile at the wavelength of the $K\alpha$ line (averaged over a 10-eV interval around the line center) is also

shown and is discussed later. Figure 72.11 shows the net core emission after subtraction of the coronal emission from the continuum profile in Fig. 72.10. To remove the effect of the slit, the derivative of the slit image is taken near the two slit edges (Schlieren). Figure 72.11 shows the result of the differentiation; as seen, the slit is wide enough with respect to the core size for the two images to be completely separated. In Fig. 72.11, neither the slit image nor its derivative has been smoothed (except for the averaging of the former over a 0.2-keV spectral interval). The full-widths at half-maximum (FWHM) of the two resulting images in Fig. 72.11 are marked in the figure; the two values, 46 μm and 44 μm , agree closely. We further compare the core emission profile obtained in Fig. 72.11 with that obtained by the dispersed images of the 5- μm -resolution KB microscope.² Although the shape of the time-integrated emission in the zeroth-order image indicates a nonuniform

implosion, this is nearly eliminated by the convolution of space and spectrum in the diffracted emission. It is possible, however, to estimate the size of the core emission region by taking a lineout through the diffracted emission. In Fig. 72.12 we show one section of the core profile derived in Fig. 72.11 (which was obtained from an image averaged around the $K\alpha$ line) and a lineout at 4.3 keV through the dispersed KB-microscope image. The difference in units is immaterial for this comparison. The average FWHM of the core size from Figs. 72.11 and 72.12 is thus $\sim 45 \mu\text{m}$.

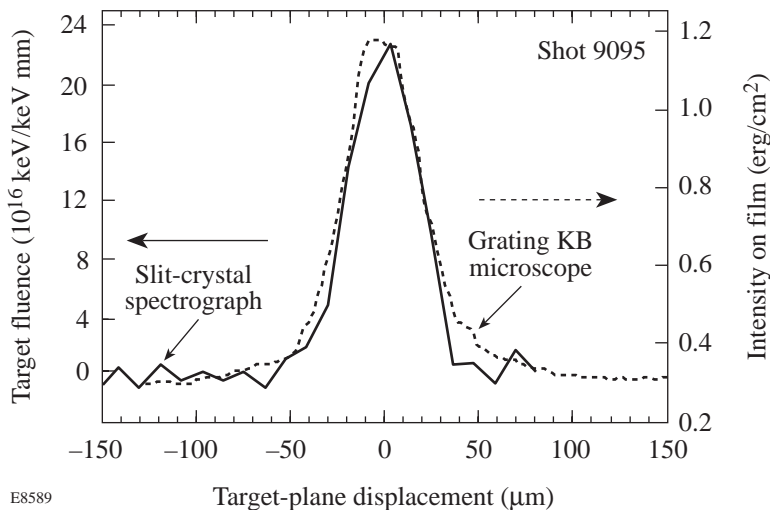
We now study the spatial profile of the $K\alpha$ line. Figure 72.13 shows the spectrum emitted at various distances from the axial view, after subtraction of the background due to the coronal emission (for clarity, the lowest spectrum was shifted down from its zero-level position). Continuous core emission, as



E8583

Figure 72.11

The continuum core emission profile (from Fig. 72.10) after subtraction of the coronal emission. The derivative of the image near the two slit edges (Schlieren) yields the core emission profile. The FWHM's of the two images are marked in the figure.



E8589

Figure 72.12

Comparison of the continuum core emission profiles obtained by two instruments: (a) KB microscope images dispersed by a transmission grating, lineout at 4.3 keV, and (b) crystal spectrograph with a slit, averaged over a 0.2-keV interval around the $K\alpha$ line (from Fig. 72.11). The difference in units is immaterial for the comparison.

well as absorption and He- α lines, is observed only close to the axial view. On the other hand, the $K\alpha$ line, emitted by the cold titanium-doped layer, is seen to come from a much wider area around the hot core. Since the local $K\alpha$ emission depends only on the cold shell density (not its temperature), its two-dimensional image can reflect directly the shell uniformity. The He- α line is indicative of mixing,⁴ which is outside the scope of this work. Suffice it to say that the spatial profile of this line as seen in Fig. 72.13 clearly shows that the mixing occurs close to the core, i.e., during the shell deceleration rather than during the acceleration phase. To obtain the net $K\alpha$ spatial profile we could use the difference between the two curves in Fig. 72.10. However, a more reliable method is to examine a large number of spectra like those in Fig. 72.13 and for each to integrate over the spectral profile of the $K\alpha$ line to obtain its total energy. The results of the latter method are shown as points in Fig. 72.14 and compared with the core emission profile as obtained from

the continuum radiation. Clearly, the $K\alpha$ -emitting cold shell is considerably larger than the core; it has a FWHM of $\sim 250 \pm 20 \mu\text{m}$. The bars show typical errors in determining the $K\alpha$ energy from the spectrum. However, the scatter of the points is greater than the error bars, indicating significant shell nonuniformity, and even asymmetry with respect to the center. Because of these limitations we can use only the $K\alpha$ profile to determine the average outer extent of the cold shell. Studying the inner extent of the cold shell would require it to be highly spherical and uniform. In that case, the Abel inversion would be applied (after deconvolution of the slit broadening); a flat-top profile would correspond to a hollow shell of radial emission.²⁰ Alternatively, a target where the doping includes the mandrel layer can be chosen (the part that forms the hot core does not emit $K\alpha$ radiation). In that case, the difference in width between the two curves in Fig. 72.14 would give directly the thickness of the cold doped layer.

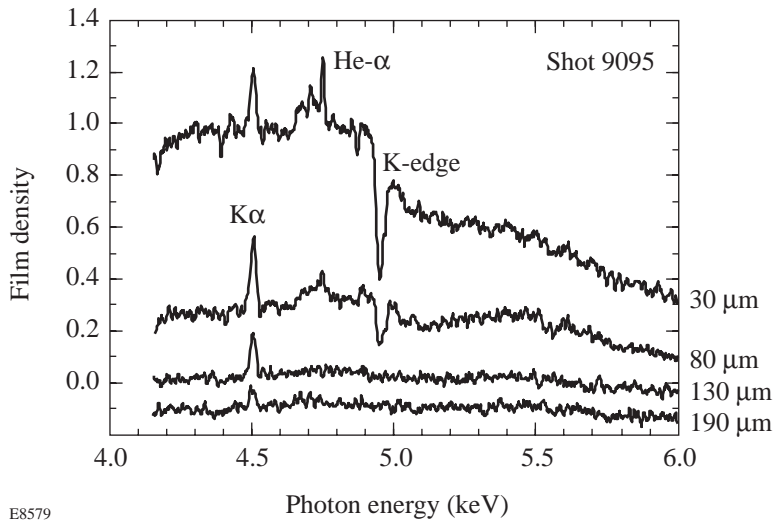


Figure 72.13

The spectra emitted at various distances from the axial view (after subtraction of the background due to coronal emission). Continuous core emission, as well as absorption and He- α lines, is emitted only close to the axial view. However, the $K\alpha$ line, emitted by the cold titanium-doped layer, is seen to come from a much wider area around the hot core. For clarity, the lowest spectrum has been shifted down from the zero-level position.

E8579

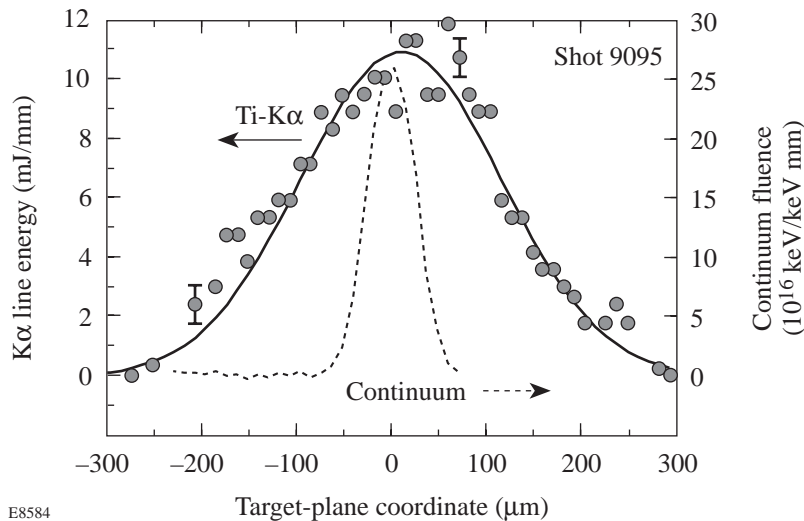


Figure 72.14

The spatial profile of the energy in the Ti $K\alpha$ line as measured by the spectrograph slit. The data points were obtained from lineouts such as in Fig. 72.13 and were fitted by a Gaussian curve. The spatial profile of the core emission (from Fig. 72.11) is shown for comparison. The cold, $K\alpha$ -emitting region is seen to be considerably wider than the core.

E8584

The outer extent of the cold shell is derived from the measured profile in Fig. 72.14, after unfolding the broadening by the slit. Figure 72.14 shows that the data points can be approximately represented by a Gaussian function, which we use merely to facilitate the deconvolution. The net profile of target emission $P_T(x)$ can be obtained from the measured profile $P_M(x)$ through the relationship

$$dP_M(x)/dx = P_T(x+d) - P_T(x-d), \quad (3)$$

where the slit width is $2d$. To solve this equation one starts at one end of the image where $P_T(x-d)$ is negligible and $P_T(x+d) \sim dP_M(x)/dx$, then moves successively through the rest of the image. The resulting FWHM of the deconvoluted image is found to be $\sim 235 \pm 20 \mu\text{m}$. The fitted curve in Fig. 72.14 is required merely for obtaining a smooth derivative in Eq. (3), but we could simply estimate a FWHM based on the experimental points and then subtract the slit width in quadrature, namely $(250^2 - 100^2)^{1/2} \sim 230 \mu\text{m}$; the two results are seen to be very similar. The diameter calculated here relates to the doped layer, including the cold mandrel it encompasses, but excluding the remainder of the compressed shell that is outside the doped layer (these three layers have comparable thicknesses).

It should be noted that the radial extent of $K\alpha$ emission in this experiment is not limited by radiation-pump depletion. This is evident in Fig. 72.9, where K -shell absorption reduces the pump intensity by less than $\sim 30\%$. Also, in the case of pump depletion the curve corrected for titanium absorption would not be a smooth exponential curve. The centrally peaked $K\alpha$ spatial profile provides an additional indication that it is excited by core radiation: a coronal source would produce a profile that decreases toward the center.

We can now obtain a rough estimate of the density of the compressed shell as follows: subtracting the core size ($45 \mu\text{m}$) from the diameter of the doped layer ($230 \mu\text{m}$) we obtain $92 \mu\text{m}$ for the thickness of the combined mandrel and doped layers. We deduced above the $\rho\Delta r$ of the total compressed shell from that of the doped layer. Similarly, we estimate here the $\rho\Delta r$ of the combined mandrel and doped layer, $\rho\Delta r(md)$, from that of the doped layer alone, $\rho\Delta r(d)$, found above to be 16 mg/cm^2 . Using the ratio $\rho\Delta r(md)/\rho\Delta r(d)$ in the initial target, namely, 1.7, we find for the compressed shell $\rho\Delta r(md) = 27 \text{ mg/cm}^2$. Coupled with the $92\text{-}\mu\text{m}$ thickness found above for the combined mandrel and doped layer we finally obtain $\rho \sim 2.9 \text{ g/cm}^3$ for the average density of the compressed shell, or a compression by a factor of ~ 2.7 . Because of the approxima-

tions involved, this estimate of the shell density has a large uncertainty ($\sim 50\%$). This uncertainty is large because the $K\alpha$ image is time integrated; thus it is unknown to what extent the sloping curve is due to a density gradient or to smearing in time. In a recent experiment,⁴ a pure titanium layer embedded within a thinner shell ($20 \mu\text{m}$) was shown (using an EXAFS spectrum) to compress by about a factor of 1.4 ± 0.15 . As explained above, an improved estimate can be obtained by extending the doping to the inner target surface; in that case, the inner radius of the cold shell would simply be given by the measured radius of the hot core. The relatively low shell compression measured here is the result of the low laser-irradiation uniformity; as mentioned above, distributed phase plates¹³ were not used in this experiment.

The relatively large emission region of the $K\alpha$ line should be reflected in a broader spectral profile (i.e., in the dispersion direction). Indeed, Fig. 72.7 shows that the $K\alpha$ line has a larger linewidth ($\sim 16 \text{ eV}$) than that of the He- α line ($\sim 8 \text{ eV}$) mainly because the latter is emitted in the hot core, whereas the former is emitted in the cold shell surrounding the core; the possible broadening of the $K\alpha$ line because of the shift with successive ionizations was shown above to be less than $\sim 5 \text{ eV}$. The source-size broadening for these lines is given by $\Delta E(\text{eV}) \sim 0.037 D (\mu\text{m})$ in terms of the emission region size D . However, this size cannot be reliably derived from this relation because of the additional broadening, which must be subtracted out before applying this relationship (this includes broadening due to the crystal, $\sim 2.5 \text{ eV}$,²¹ and the natural linewidth, which for the $K\alpha$ is $\sim 4.5 \text{ eV}$).²²

4. Core Density Derived from the Continuum Intensity

An additional diagnostic is provided by the absolute intensity of the continuum radiation from the core. Knowing the core temperature and the volume and duration of the core emission, we can derive the compressed-core density and compare it with the shell density derived above. The absolute intensity can be reliably determined since the crystal calibration agrees well with theoretical calculations.⁴ The continuum core emission is due to bremsstrahlung (free-free) and recombination (free-bound) radiations of the CH core. At the core temperature ($\sim 1 \text{ keV}$) the hydrogen and carbon ions are fully ionized and the emission at an energy E into the total solid angle, per unit volume, time, and photon-energy interval, can be shown to be²³

$$\varepsilon(10^{16} \text{ keV/keV ns } \mu\text{m}^3) = 1.7 \times 10^{-4} \exp(-E/T) \left[\rho^2 / T^{1/2} \right] \left[1 + (2E_i/T) \exp(E_i/T) \right]. \quad (4)$$

Here, E_i is the ionization energy of C^{+5} (0.49 keV) and T is the temperature in keV. The second term in brackets is the ratio of free-bound to free-free radiation intensities. We choose in Eq. (4) $E = 4.5$ keV (i.e., the continuum underlying the $K\alpha$ line). The Gaunt correction factors are very close to 1 when $E/E_i \gg 1$ (here $E/E_i = 9.2$). The imaging streak camera showed that the time history of core emission has a FWHM of ~ 0.25 ns. With the measured core temperature of 1.1 keV, the time-integrated emission ϵ_t is

$$\epsilon_t (10^{16} \text{ keV/keV } \mu\text{m}^3) = 1.6 \times 10^{-6} \rho^2. \quad (5)$$

The measured time- and space-integrated emission at 4.5 keV is $\sim 1 \times 10^{16}$ keV/keV, after subtracting the coronal emission (see Fig. 72.9). This value has to be corrected for the attenuation through the cold shell. From the shell areal density measured above we find this attenuation to be by a factor of ~ 2.5 ; thus, the net emission is $\sim 2.5 \times 10^{16}$ keV/keV. The profile of the one-dimensional image (Fig. 72.12) can be approximated by a Gaussian of FWHM of $\Delta = 45 \mu\text{m}$. Assuming the core emission is isotropic, the peak emission per unit volume can be shown to be related to the volume-integrated emission through

$$\text{peak emission} = 8(\ln 2/\pi)^{3/2} (\text{total emission}/\Delta^3). \quad (6)$$

Combining Eqs. (5) and (6) we find a core density of $\sim 4 \pm 1 \text{ g/cm}^3$. The areal density corresponding to the FWHM of the continuum spatial profile is $\sim 17 \pm 4 \text{ mg/cm}^2$.

5. Summary of Derived Shot Parameters

Table 72.I summarizes the diagnostic results for shot 9095 analyzed in this work, and the methods used in their derivation. For comparison, the table also lists the corresponding results for shot 8207, which was the subject of analysis described in Ref. 4. The two shots are different in several important respects but yield comparable results: shot 8207 had a thinner shell ($20 \mu\text{m}$ as compared with $33.5 \mu\text{m}$) and a lower laser energy (20 kJ as compared with 30 kJ). Also, shot 8207 had a thin layer ($0.3 \mu\text{m}$) of pure titanium as compared with a thick layer ($8.7 \mu\text{m}$) of 0.5%-doped CH. The $K\alpha$ analysis in this work was not applied to shot 8207 because the $K\alpha$ line was outside the measured spectral range (see Fig. 4 in Ref. 4). Also, the EXAFS analysis of Ref. 4 was not applied to shot 9095 in this work because EXAFS data for a doped polymer (rather than a pure metal) is not known. The results given in Table 72.I show that spectral data can provide very useful and wide-ranging information of target behavior.

Conclusions

In summary, a diagnostic method is proposed for imaging the cold, compressed shell of imploding targets using high-Z doping and imaging the $K\alpha$ fluorescence. Two-dimensional

Table 72.I: Summary of diagnostic results and methods used for shots 8207 and 9095.

	Shot 8207	Shot 9095
Core temperature	0.94 keV Continuum slope	1.1 keV Continuum slope
Shell $\rho\Delta r$	$>17 \text{ mg/cm}^2$ K -edge absorption, absorption lines	$>42 \text{ mg/cm}^2$ K -edge absorption
Shell compression ratio (ρ/ρ_0)	1.4 ± 0.15 EXAFS	2.7 ± 1.3 $K\alpha$ spatial profile
Doped-shell temperature range	$\sim 10 \text{ eV}$ to $\sim 300 \text{ eV}$ K -edge absorption, absorption lines	$<40 \text{ eV}$ K -edge absorption
Core density Core areal density	$7 \pm 2 \text{ g/cm}^3$ $32 \pm 8 \text{ mg/cm}^2$ Continuum intensity and core size	$4 \pm 1 \text{ g/cm}^3$ $17 \pm 4 \text{ mg/cm}^2$ Continuum intensity and core size
Mixing	He- α line emission	He- α line emission

imaging and time gating would greatly enhance the usefulness of the method. However, even one-dimensional, time-integrated images can yield the average outer extent of the cold shell around the time of peak compression. An advantage of one-dimensional, polychromatic imaging is that the spectrum of the $K\alpha$ line (including the underlying continuum) can be measured with high spectral resolution and the net $K\alpha$ emission can be reliably determined. The present results show that adequate $K\alpha$ intensity can be obtained with a low level of doping, which minimizes target-behavior modification. The $K\alpha$ emission signature studied in this work should prove very useful in tracking the improved target performance with improved laser uniformity. Additionally, the measured absolute intensity of continuum x rays from the core can be reliably used to estimate its density and areal density.

ACKNOWLEDGMENT

This work was supported by the U.S. Department of Energy Office of Inertial Confinement Fusion under Cooperative Agreement No. DE-FC03-92SF19460, the University of Rochester, and the New York State Energy Research and Development Authority. The support of DOE does not constitute an endorsement by DOE of the views expressed in this article.

REFERENCES

1. B. Yaakobi, R. Epstein, and F. J. Marshall, Phys. Rev. A **44**, 8429 (1991).
2. F. J. Marshall, J. A. Delettrez, R. Epstein, and B. Yaakobi, Phys. Rev. E **49**, 4381 (1994).
3. B. Yaakobi, R. S. Craxton, R. Epstein, and Q. Su, J. Quant. Spectrosc. Radiat. Transfer **58**, 75 (1997).
4. B. Yaakobi, F. J. Marshall, D. K. Bradley, J. A. Delettrez, R. S. Craxton, and R. Epstein, Phys. Plasmas **4**, 3021 (1997).
5. S. G. Glendinning *et al.*, in *Applications of Laser Plasma Radiation II*, edited by M. C. Richardson and G. A. Kyrala (SPIE, Bellingham, WA, 1995), Vol. 2523, pp. 29–39; D. H. Kalantar *et al.*, Bull. Am. Phys. Soc. **40**, 1856 (1995); D. H. Kalantar *et al.*, Rev. Sci. Instrum. **68**, 814 (1997).
6. H. Nishimura *et al.*, Phys. Fluids **31**, 2875 (1988).
7. J. S. Wark *et al.*, Appl. Phys. Lett. **48**, 969 (1986).
8. See, e.g., B. Yaakobi, I. Pelah, and J. Hoose, Phys. Rev. Lett. **37**, 836 (1976); A. Hauer, W. Priedhorsky, and D. van Hulsteyn, Appl. Opt. **20**, 3477 (1981); J. D. Hares *et al.*, Phys. Rev. Lett. **42**, 1216 (1979).
9. See, e.g., J. Mizui *et al.*, Phys. Rev. Lett. **39**, 619 (1977); B. Yaakobi, J. Delettrez, L. M. Goldman, R. L. McCrory, W. Seka, and J. M. Soures, Opt. Commun. **41**, 355 (1982).
10. F. J. Marshall and J. A. Oertel, Rev. Sci. Instrum. **68**, 735 (1997).
11. T. R. Boehly, R. S. Craxton, T. H. Hinterman, J. H. Kelly, T. J. Kessler, S. A. Kumpan, S. A. Letzring, R. L. McCrory, S. F. B. Morse, W. Seka, S. Skupsky, J. M. Soures, and C. P. Verdon, Rev. Sci. Instrum. **66**, 508 (1995).
12. Laboratory for Laser Energetics LLE Review **37**, 29, NTIS document No. DOE/DP/40200-83 (1988); *ibid.*, p. 40. Copies may be obtained from the National Technical Information Service, Springfield, VA 22161.
13. Laboratory for Laser Energetics LLE Review **33**, 1, NTIS document No. DOE/DP/40200-65 (1987). Copies may be obtained from the National Technical Information Service, Springfield, VA 22161.
14. D. Denley *et al.*, Phys. Rev. B **19**, 1762 (1979); G. Blanche *et al.*, J. Phys. IV **4**, 145 (1994).
15. P. A. Lee *et al.*, Rev. Mod. Phys. **53**, 769 (1981).
16. L. L. House, Astrophys. J. Suppl. **18**, 21 (1969).
17. P. Suortti, J. Appl. Phys. **42**, 5821 (1971).
18. D. Duston *et al.*, Phys. Rev. A **27**, 1441 (1983).
19. E. J. McGuire, Phys. Rev. **185**, 1 (1969).
20. C. M. Vest and D. G. Steel, Opt. Lett. **3**, 54 (1978).
21. A. J. Burek and B. Yaakobi, Final Report to the National Bureau of Standards contract NB81NAHA2032 (1983) (unpublished), Appendix A.
22. E. J. McGuire, Phys. Rev. A **2**, 273 (1970).
23. H. R. Griem, *Plasma Spectroscopy* (McGraw-Hill, New York, 1964), Chap. 5.